Towards Accurate Three-Dimensional Simulation of Dense Multi-Phase Flows Using Cylindrical Coordinates

A. Bakshi*, C. Altantzis, A.F. Ghoniem

Massachusetts Institute of Technology, Department of Mechanical Engineering
77 Massachusetts Ave., Cambridge, MA 02139, United States

Abstract

Most industrial scale fluidized-bed reactors are cylindrical, and the cylindrical coordinate system is a natural choice for their CFD simulation. There are, however, subtle complexities associated with this choice when using the Two-Fluid Model. The center of the grid forms a computational "boundary" and requires special treatment. Conventionally, a free slip no-normal flow condition has been used which does not predict the hydrodynamics accurately even when predicted parameters are in good agreement with measurement. Another difficulty is posed by the extremely small cells near the grid center, especially when simulating small scale experiments. The presence of these small cells raises concerns over the applicability of the Two-Fluid Model and is known to result in slow simulation convergence. These issues are addressed in the present study and appropriate solutions are proposed including the centerline treatment and the use of a non-uniform grid. Finally, the study compares the Cartesian grid with the cylindrical grid for application to fluidization. It is shown that simulating a cylindrical bed using the cylindrical grid is not only more accurate but also more computationally efficient. The analysis presented along with the proven computational efficiency of the cylindrical grid is especially significant considering that modeling commercial scale reactors, with multiple solid phases and chemical reactions, will not only require accurate description of the fluidization process but will also be exceedingly expensive in terms of computational cost.

Keywords: Fluidized bed, two-fluid model, three-dimensional, cylindrical coordinates, non-uniform grid

1. Introduction

Fluidized bed technology is employed in a variety of industrial operations in the chemical and petroleum industries. Gas-solid fluidization is especially suitable for large-scale operations since it provides distinctly high heat and mass transfer rates as compared to other means of contacting [1]. However, despite their extensive usage, performance optimization continues to be an expensive and complicated task since most fluidized beds operate at high pressures and temperatures and involve chemical reactions. Hence, one of the key aspects concerning the design of commercial fluidized beds is the advancement of Computational Fluid Dynamics (CFD) to complement the experimental investigation as a means to understand the flow hydrodynamics and optimize the operation.

Solid-gas flows can be modeled using a combination of Lagrangian and Eulerian models. The most common frameworks for industrial scale applications are the Eulerian-Eulerian framework or the Two Fluid Model (TFM), where the gas and solid phases are considered as inter-penetrating continua [2–5], and the Lagrangian-Eulerian framework or the Discrete Particle Model (DPM), where the solid phases consist of particles interacting with a continuous gas phase [6–8]. The TFM is efficient and can describe multi-phase flow at relatively large scales, unlike the DPM, where computational demands limit the number of solid-phase particles that can be used, making the approach only feasible for dilute solid-phase flows [9]. On the other hand, the former requires closure laws to incorporate particle-particle and particle-gas interactions into the continuum model, making the modeling more complex [10].

One consequence of using the continuum model for the solid phase is the need to define solid phase pressure and viscosity, i.e. the solid phase stress tensor, analogous to the fluid stress tensor in Navier-Stokes equations

---

*Corresponding Author
Email address: abakshi@mit.edu, Telephone number: +1 (617) 459-1318

for describing single-phase fluid flow. The computation of this solid phase stress tensor should be based on the local packing fraction, since the particle flow mechanism is different for dilute and dense flows. For dilute flows, collisional stresses predominate and the flow can be modeled using the kinetic theory of granular flow [11–13] while for densely packed regions, frictional stresses must be appropriately accounted for [14]. Another complexity in the TFM is to model the particle-gas drag force for which several models have been proposed in literature [2, 15]. Using these constitutive relationships, the mass, momentum and energy equations can be solved along with the transport equation for granular temperature to completely describe solid-gas flow. Granular temperature is a measure of the specific kinetic energy of the random fluctuating component of the particle velocity and can be generated or transferred through convection, diffusion and dissipation just like any other scalar property [16].

Despite the computational advantage of the TFM, most fluidized beds have conventionally been simulated in 2D. This is because 2D simulations are relatively inexpensive as compared to full scale 3D simulations. However, restricting the domain to two dimensions assumes an infinitely long span, an assumption which is questionable considering that most experimental data has been obtained from thin fluidized beds because of the ease of optical accessibility [9, 17–19]. In such "pseudo-2D" laboratory and small-scale experiments, wall effects (particularly the particle-wall friction) play a critical role in the bubble dynamics [20, 21]. Another issue has been the choice of coordinate system for modeling fluidized beds, especially industrial reactors, most of which are cylindrical. Using the 2D cylindrical coordinate system necessitates the use of an axi-symmetric boundary condition, which does not represent a real fluidized bed accurately. Therefore, several researchers have worked with the 3D cylindrical coordinate system [9, 22–26]. Interestingly, modeling a 3D cylindrical bed as an axial slice around the axis of the bed using 2D Cartesian coordinates has predicted bed parameters in good agreement with experimental data for bubbling fluidization. Even though the governing equations for the 3D cylindrical coordinate system significantly differ from the 2D Cartesian coordinate system, it has been shown that the additional terms in the former are insignificant as compared to the terms in common. However, with increasing inlet superficial gas velocity, there is significant lateral flow variation and hence, increasing disparity between the 2D Cartesian and 3D Cylindrical simulations [22]. Such reduced-dimension scaling may also not be possible for reactive simulations [23] or significantly asymmetric geometries [24]. With growing emphasis on mixing and segregation studies, 2D beds should not be used to validate numerical models.

Recently, 3D Cartesian grids have been used to simulate complex geometries, including cylindrical beds, using the Cut-Cell approach, replacing the conventional staircase modeling of the boundary with boundary cells having curved or sloping boundaries [27]. In this study, we show that simulating bubbling fluidization in cylindrical beds using cylindrical grids is not only more accurate but also computationally more efficient than the Cartesian grid. The superior accuracy of the cylindrical grid is because its computational grid perfectly aligns with the physical boundary eliminating any boundary approximations whatsoever. On the other hand, the azimuthal resolution may be relaxed in favor of higher radial resolution [22, 28] making the cylindrical grid more efficient, unlike the Cartesian grid where both cross-sectional axes must be equally well-resolved. The use of the cylindrical grid, however, requires special treatment at the center (origin) of the domain. This difficulty at r=0 is purely a numerical artifact, and hence, must be appropriately handled. Conventionally, a free-slip no-normal flow condition has been imposed. This condition effectively models a *wall* at the center of the bed, the presence of which obstructs the flow of solid particles and subsequently, repels the flow of gas bubbles [28, 29]. Both these phenomena act simultaneously and result in excess solid holdup at the center of the bed. Although bed parameters like the pressure drop and bed height are still predicted in reasonable agreement with measurements [9, 24], the predicted hydrodynamics at the center of the bed do not compare well.

The no-normal flow condition has been well documented in literature, albeit for single-phase turbulent flow [30–32]. Most of these studies have been limited to DNS/LES codes based on Finite Difference Method (FDM). A major concern with the use of FDM for simulating cylindrical grids, besides the centerline boundary condition, is the treatment of the *pole singularity*; since differential operators blow up as the radial grid approaches r→0. As a remedy, solution algorithms often modify the governing equations. Constantinescu and Lele [30] proposed a highly accurate algorithm based on a combination of mesh restructure and application of general series expansions around the *pole*. Using similar techniques, Fukagata and Kasagi [31] derived a first order energy conservative centerline boundary condition, besides using mixed interpolation schemes for the advection and body force terms. Morinishi et al [32] extended this approach by proposing the use of a domain-averaged Jacobian to discretize the governing equations close to the center. The present study is, however, based on the Finite Volume framework on a staggered grid which uses integral operators to derive the discretized governing equations. Using integral operators coupled with the computation of fluxes at the sides of the control volume removes the pole singularity. The application of an appropriate centerline treatment,

though, is still imperative and numerically, it particularly affects the computation of the diffusion and drag force terms in the cells at the grid center. Thus, using an accurate centerline condition is not only essential for understanding the hydrodynamics of more complex flows (eg mixtures, reactive flows) but also for constructing accurate sub-grid models for coarse grid simulations [33–35]. Recently, Verma et al. [28] simulated solid-gas fluidization in a cylindrical bed using a similar approach and predicted the radial velocity using diametrical momentum averaging. They showed significant differences in the average cross-sectional bubble diameters predicted, due to splitting of bubbles at the center when using the no-normal flow condition. One drawback with their approach is that it does not predict a unique Cartesian velocity at the cross section center for either phase.

The emphasis of the present work is two-fold. An appropriate centerline treatment for the simulation of multi-phase flow using the cylindrical grid is implemented and compared to the existing free slip no-normal flow condition. The cylindrical grid is then compared to the Cartesian grid for application to solid-gas fluidization in terms of accuracy as well as computational complexity. For validation, comparisons are made with the experimental data of Makkawi et al [36]. The scheme has been implemented in MFiX (Multiphase Flow with Interface eXchanges), an open-source code developed at the National Energy Technology Laboratory, USA to describe the flow hydrodynamics in fluid-solid systems.

2. Experimental Setup

For the present study, the experiments by Makkawi et al [36] have been used to validate the numerical model. Cold fluidization was carried out in a cast acrylic cylindrical column with internal diameter 13.8 cm. Air at ambient conditions was introduced through a perforated distributor located at the bottom of the column into an initially static bed of glass ballotini particles, classified as Geldart group B type. The experiments were run for 50 s and data was collected at 100 frames per second using Electrical Capacitance Tomography (ECT). This technique uses electrical capacitance sensor rings to determine the spatial distribution of the composite permittivity of the gas-solid phase. The experiments were conducted at several inlet superficial air velocities although the present study only analyses the cases using 0.54 and 0.80 m/s corresponding to the bubbling and slugging flow regimes, respectively. The schematic of the experimental setup is shown in Figure (1) and a summary of the experimental conditions is presented in Table (1).

3. Numerical Modeling and Formulation

3.1. Governing Equations

The Two Fluid Model (TFM) is used to simulate the hydrodynamics of solid-gas fluidization. Since the TFM describes the solid phase as a continuum, the motion of the solid phase is governed by conservation equations similar to those used for single-phase fluid flow. For cold fluidization with no chemical reactions, there is no mass transfer between phases and the mass conservation equations are reduced to

$$\frac{\partial}{\partial t}\left(\varepsilon_g \rho_g\right) + \nabla \cdot \left(\varepsilon_g \rho_g \vec{V}_g\right) = 0 \tag{1}$$

$$\frac{\partial}{\partial t}\left(\varepsilon_m \rho_m\right) + \nabla \cdot \left(\varepsilon_m \rho_m \vec{V}_m\right) = 0 \tag{2}$$

where ε, ρ and $\vec{V}$ represent the volume fraction, density and velocity with the subscripts g and m denoting the gas and solid phases (m=1,M) respectively. Note that the effective density is the product of the actual density ρ and the volume fraction ε of the phase. The momentum equations

$$\frac{\partial}{\partial t}\left(\varepsilon_g \rho_g \vec{V}_g\right) + \nabla \cdot \left(\varepsilon_g \rho_g \vec{V}_g \vec{V}_g\right) = \nabla \cdot \bar{\bar{S}}_g - \varepsilon_g \nabla P_g + \varepsilon_g \rho_g \vec{g}_g - \sum_{m=1}^{M} \vec{I}_{gm} \tag{3}$$

$$\frac{\partial}{\partial t}\left(\varepsilon_m \rho_m \vec{V}_m\right) + \nabla \cdot \left(\varepsilon_m \rho_m \vec{V}_m \vec{V}_m\right) = \nabla \cdot \bar{\bar{S}}_m - \varepsilon_m \nabla P_g + \varepsilon_m \rho_m \vec{g}_m + \vec{I}_{gm} - \sum_{k=1}^{M} \vec{I}_{km} \tag{4}$$

are similar to the Navier-Stokes equations with additional terms which require closure. Specifically the mass and momentum conservation equations in the cylindrical coordinate system for the gas phase (for instance) are

given by

$$\frac{\partial (\varepsilon_g \rho_g)}{\partial t} + \frac{1}{r}\frac{\partial}{\partial r}\left(r\varepsilon_g \rho_g V_{gr}\right) + \frac{1}{r}\frac{\partial}{\partial \theta}\left(\varepsilon_g \rho_g V_{g\theta}\right) + \frac{\partial}{\partial y}\left(\varepsilon_g \rho_g V_{gy}\right) = 0$$

$$\frac{\partial (\varepsilon_g \rho_g V_{gr})}{\partial t} + \frac{1}{r}\frac{\partial \left(r\varepsilon_g \rho_g V_{gr}^2\right)}{\partial r} + \frac{1}{r}\frac{\partial \left(\varepsilon_g \rho_g V_{gr} V_{g\theta}\right)}{\partial \theta} - \frac{\rho_g \varepsilon_g V_{g\theta}^2}{r} + \frac{\partial \left(\varepsilon_g \rho_g V_{gr} V_{gy}\right)}{\partial y} = -\varepsilon_g \frac{\partial p}{\partial r}$$
$$+ \left(\frac{1}{r}\frac{\partial \left(\varepsilon_g r S_{grr}\right)}{\partial r} + \frac{1}{r}\frac{\partial \left(\varepsilon_g S_{g\theta r}\right)}{\partial \theta} - \frac{\varepsilon_g S_{g\theta\theta}}{r} + \frac{\partial \left(\varepsilon_g S_{gyr}\right)}{\partial y}\right) + \varepsilon_g \rho_g g_r - \sum_{m=1}^{M} I_{gr}$$

$$\frac{\partial (\varepsilon_g \rho_g V_{g\theta})}{\partial t} + \frac{1}{r}\frac{\partial \left(r\varepsilon_g \rho_g V_{gr} V_{g\theta}\right)}{\partial r} + \frac{1}{r}\frac{\partial \left(\varepsilon_g \rho_g V_{g\theta}^2\right)}{\partial \theta} + \frac{\rho\varepsilon_g \left(V_{gr} V_{g\theta}\right)}{r} + \frac{\partial \left(\varepsilon_g \rho_g V_{gy} V_{g\theta}\right)}{\partial y} = -\varepsilon_g \frac{1}{r}\frac{\partial p}{\partial \theta}$$
$$+ \left(\frac{1}{r^2}\frac{\partial \left(\varepsilon_g r^2 S_{gr\theta}\right)}{\partial r} + \frac{1}{r}\frac{\partial \left(\varepsilon_g S_{g\theta\theta}\right)}{\partial \theta} + \frac{\partial \left(\varepsilon_g S_{gy\theta}\right)}{\partial y}\right) + \varepsilon_g \rho_g g_\theta - \sum_{m=1}^{M} I_{g\theta}$$

$$\frac{\partial (\varepsilon_g \rho_g V_{gy})}{\partial t} + \frac{1}{r}\frac{\partial \left(r\varepsilon_g \rho V_{gr} V_{gy}\right)}{\partial r} + \frac{1}{r}\frac{\partial \left(\varepsilon_g \rho_g V_{g\theta} V_{gy}\right)}{\partial \theta} + \frac{\partial \left(\varepsilon_g \rho_g V_{gy}^2\right)}{\partial y} = -\varepsilon_g \frac{\partial p}{\partial z}$$
$$+ \left(\frac{1}{r}\frac{\partial \left(\varepsilon_g r S_{gry}\right)}{\partial r} + \frac{1}{r}\frac{\partial \left(\varepsilon_g S_{gy\theta}\right)}{\partial \theta} + \frac{\partial \left(\varepsilon_g S_{gyy}\right)}{\partial y}\right) + \varepsilon_g \rho_g g_y - \sum_{m=1}^{M} I_{gy}$$

The terms $\varepsilon_g \nabla P_g$ and $\varepsilon_m \nabla P_g$, in Equations (3) and (4), respectively, represent the buoyancy forces due to the gradient in gas (fluid) pressure P_g. Assuming no mass transfer, the solids-solids momentum transfer $(\vec{I}_{km})$ is simply the drag force between the solid particles evaluated using a simplified version of the kinetic theory [16] while the fluids-solids momentum transfer term $(\vec{I}_{gm})$ is the fluid-solid drag force (F_{gm}). The fluid-solid drag force is particularly significant for cold fluidization and the in present study, is based on the Syamlal-O'Brien model [16] given by

$$F_{gm} = \frac{3\varepsilon_m \varepsilon_g \rho_g}{4\left(V_{rm}\right)^2 d_{pm}} C_{Ds} \left(\frac{Re_m}{V_{rm}}\right) |\vec{V}_m - \vec{V}_g| \tag{5}$$

based on the particle diameter d_{pm} and the single-sphere drag function C_{Ds}. V_{rm} is the terminal velocity correlation for the mth solid phase and the Reynolds number Re_m is given by

$$Re_m = \frac{d_{pm}|\vec{V}_m - \vec{V}_g|\rho_g}{\mu_g} \tag{6}$$

A final closure is required for the computation of the stress tensors $(\bar{\bar{S}})$. The computation of the gas phase stress tensor $\bar{\bar{S}}_g$ is identical as in single-phase fluid flow. On the other hand, the closure law for the solid phase stress tensor $\bar{\bar{S}}_m$ is based on the granular flow regime, i.e. the local packing fraction of the solid phase(s). The viscous regime is characterized by stresses arising from collisions between particles making it predominant in the dilute pockets of the bed. These collisions are inelastic and dissipate the kinetic energy of the particles. The presence of mean and fluctuating components of the velocity field also make this flow regime analogous to single phase turbulent compressible flow [11]. Meanwhile, densely packed regions are associated with plastic flow, i.e. the particle have more enduring contact and hence, frictional stress between the sliding particles predominates. The stress tensor evaluation for the two regimes is blended using a hyperbolic tangent function around the critical void fraction ε_g^* which is typically the maximum possible solid packing [9]. Thus, in its general form, the stress tensor can be written as follows:

$$\bar{\bar{S}}_m = \begin{cases} -P_m^p \bar{\bar{I}} + \bar{\bar{\tau}}_m^p & \text{if } \varepsilon_g \leq \varepsilon_g^* \\ -P_m^v \bar{\bar{I}} + \bar{\bar{\tau}}_m^v & \text{if } \varepsilon_g > \varepsilon_g^* \end{cases} \tag{7}$$

where P_m is the pressure and $\bar{\bar{\tau}}_m$ is the viscous stress in the mth solid phase. The superscripts p and v stand for the plastic and viscous regimes. The computation of the solid stress tensor is critical to maintaining the incompressibility of the solid phase and hence, key to the numerical stability of fluidization simulations.

The solid phase pressure and viscosity are both functions of the granular temperature Θ [16]. The granular

4

energy transport equation given by

$$\frac{3}{2}\left(\frac{\partial(\varepsilon_m\rho_m\Theta_m)}{\partial t} + \nabla\cdot\left(\varepsilon_m\rho_m\vec{V}_m\Theta_m\right)\right) = \bar{\bar{S}}_m : \nabla\vec{V}_m + \nabla\cdot\vec{q}_{\Theta_m} - \gamma_{\Theta_m} + \phi_{gm} + \sum_{\substack{l=1 \\ l\neq m}}^{M}\phi_{lm} \tag{8}$$

can be used to solve for Θ_m. In addition to the transient and convective terms on the left, the terms in the equation include the production ($\bar{\bar{S}}_m : \nabla\vec{V}_m$), diffusional flux ($\nabla\cdot\vec{q}_{\Theta_m}$), dissipation through inelastic collisions (γ_{Θ_m}), viscous dissipation due to fluid viscosity (ϕ_{gm}) and the transfer of granular energy between phases (ϕ_{lm}). Neglecting the convection and diffusion components, this equation can be simplified and reduced to the following algebraic equation:

$$\Theta_m = \left(\frac{-K_{1m}\varepsilon_m tr\left(\bar{\bar{D}}_m\right) + \sqrt{\left(K_{1m}\varepsilon_m tr\left(\bar{\bar{D}}_m\right)\right)^2 + 4K_{4m}\varepsilon_m\left(K_{2m}tr^2\left(\bar{\bar{D}}_m\right) + 2K_m tr\left(\bar{\bar{D}}_m^2\right)\right)}}{2\varepsilon_m K_{4m}}\right)^2 \tag{9}$$

where K_{1m}, K_{2m}, K_{3m} and K_{4m} are constants determined using the Kinetic Theory of Granular Flow (KTFG). The algebraic equation is more convenient to implement since it is an explicit expression to evaluate the granular temperature although predictions using this approximation are less accurate close to the walls because boundary conditions are not appropriately satisfied. For the present study, the full transport equation given by Equation (8) has been used for all simulations presented in Sections 4.1 and 4.2, whereas the simplified algebraic equation, given by Equation (9), has been used for all simulations presented in Section 4.3 since the implementation of the former on the Cartesian grid is still in progress.

The Multiphase Flow with Interface eXchanges (MFiX) code developed at the National Energy Technology Laboratory, USA is used for simulating the Eulerian-Eulerian model and implementing the closure laws for the particle-particle and the particle-gas interactions. More details regarding the governing equations, the constitutive relations and their implementation can be found in [16, 37].

3.2. Domain Discretization

For the present study, both the cylindrical and Cartesian grids are used to simulate the fluidization hydrodynamics for the cylindrical bed. As is evident from Figure (2a), the cylindrical grid perfectly aligns with the physical boundary. On the other hand, the Cartesian grid using the Cartesian Cut-Cell technique as shown in Figure (2b), makes use of truncated cells to conform to the curved boundary of the fluidized bed while very small cells are discarded from the domain altogether. This makes modeling a cylindrical or any non-Cartesian bed using the Cartesian grid complex. More details on the Cartesian cut-cell implementation can be found in [27].

One aspect concerning simulations of solid-gas flows, especially using the cylindrical grid, is the grid resolution. Very coarse grids may not predict the hydrodynamics accurately [38, 39] while slow convergence has been previously reported for simulations employing very fine cylindrical grids because of the presence of extremely small cells at the grid center [28]. For instance, the center-cell volume is only about 5 % of the circumference-cell volume in Figure (2a). Presence of such small cells may violate the continuum model for the solid phase i.e. the solid phase flow may no longer be described by volume-averaged properties.

Celmins [40] derived an empirical formula for the lower bound on the averaging volume for the spatially averaged description of two-phase flow. Considering m spherical particles of diameter d occupying the domain volume W, the average gas volume fraction (in W) is given by

$$\bar{\alpha} = 1 - \frac{\pi}{6}\frac{md^3}{W} \tag{10}$$

The mean free distance between particle centers L_m can be estimated by representing the average volume per particle W/m as a sphere of diameter L_m i.e.

$$\frac{W}{m} = \frac{4}{3}\pi\left(\frac{L_m}{2}\right)^3 \tag{11}$$

Combining equations (10) and (11), we obtain

$$L_m = d \left(1 - \bar{\alpha}\right)^{-1/3} \tag{12}$$

For any averaging sphere of arbitrary volume V, the gas volume fraction inside the sphere α is a function of the location X and radius R of the sphere as well as the average gas volume fraction $\bar{\alpha}$ inside the domain volume W i.e.

$$\alpha = f \left(\frac{X}{L_m}, \frac{R}{L_m}, \bar{\alpha}\right) \tag{13}$$

Based on numerical simulations on four lattices (square cylinder, triangular cylinder, leap-frog square and leap-frog triangular lattices) having different symmetries and maximal packing densities $\bar{\alpha}_{min} \in [0.260, 0.476]$, Clemins showed that the undulation in α about the limit $\bar{\alpha}$, for any X, can be bounded by

$$|\Delta\alpha| = |\alpha - \bar{\alpha}| < 0.5\bar{\alpha}^2 \left(1 - \bar{\alpha}\right) \left(\frac{L_m}{R}\right)^2 \tag{14}$$

Physically, for extremely small averaging volumes ($R/L_m < 1$), α oscillates significantly about $\bar{\alpha}$ whereas for large averaging volumes ($R/L_m \sim 4$), changes in α are negligible i.e. $\alpha \to \bar{\alpha}$. Conversely, for a fixed averaging volume (i.e. fixed R), increasing the number of particles inside the averaging volume V decreases the mean free distance and hence, the error ($\alpha - \bar{\alpha}$) in the gas volume fraction. This is also intuitive since capturing more particles within the control volume should result in a more accurate description of the flow field using spatial averaging. Keeping most practical applications in mind, this formula has been derived for the range $\alpha \in [0.5, 1.0]$ and $R/L_m \geq 1$. The analysis also assumes homogeneous distribution of particles, i.e. no obvious particle clusters, periodic or random, inside the averaging volume, an assumption in tune with the modeling assumption of the TFM.

Equation (14) can be re-expressed as

$$\frac{R}{L_m} > \bar{\alpha} \left(\frac{1 - \bar{\alpha}}{2|\Delta\bar{\alpha}|_{tol}}\right)^{1/2} \tag{15}$$

where $|\Delta\bar{\alpha}|_{tol}$ is the maximum allowable error in the void fraction and is given by

$$|\Delta\bar{\alpha}|_{tol} = \begin{cases} |\Delta\bar{\alpha}|_t & \bar{\alpha} \leq \bar{\alpha}_t \\ \dfrac{1 - \bar{\alpha}}{1 - \bar{\alpha}_t} |\Delta\bar{\alpha}|_t & \bar{\alpha}_t < \bar{\alpha} \end{cases} \tag{16}$$

where $\bar{\alpha}$ and $|\Delta\bar{\alpha}|_t$ are introduced to tune the tolerance for $\bar{\alpha}$ approaching unity. More details regarding this analysis can be found in [40].

Extending this analysis to cylindrical grids such that cells at the grid center be represented as spheres of radius R, the constraint given by Equation (15) can now be re-expressed as

$$(\Delta r)^2 \times \Delta\Theta \times \Delta y \geq \frac{8\pi}{3} d^3 \bar{\alpha}^3 \times \left(max \left(1 - \bar{\alpha}, 1 - \bar{\alpha}_t\right)\right)^{\frac{1}{2}} \left(\frac{1}{2|\Delta\bar{\alpha}|_t}\right)^{\frac{3}{2}} \tag{17}$$

or likewise, for the Cartesian grid as

$$\Delta x \times \Delta z \times \Delta y \geq \frac{4\pi}{3} d^3 \bar{\alpha}^3 \times \left(max \left(1 - \bar{\alpha}, 1 - \bar{\alpha}_t\right)\right)^{\frac{1}{2}} \left(\frac{1}{2|\Delta\bar{\alpha}|_t}\right)^{\frac{3}{2}} \tag{18}$$

Using $|\Delta\bar{\alpha}|_t = 0.01$ and $\bar{\alpha}_t$ close to 1 (say 0.85, as suggested by Clemins [40]), it can be easily verified from Equation (18) that a grid resolution of atleast 8 particle diameters is required while simulating solid-gas flows ($\bar{\alpha} \in [0.4, 1]$) using Cartesian grids. Also note that this constraint is less stiff than the one given by Equation (17) for the cylindrical grid because of the significantly smaller cell volumes at the domain center using the latter; the difference is almost 4 times for the grids shown in Figure (2).

A subtle complexity, however, with this approach, which can be seen in Equations (17) and (18), is the dependence of the critical grid resolution on the average void fraction $\bar{\alpha}$. Recognizing that access to experimental data may often be limited, choosing the grid resolution should, therefore, be based on an *expected* void fraction

profile; an assumption which could be verified post-simulation. Another approximation could be to design the grid based on $\bar{\alpha} = 2/3$ since this corresponds to the maximum deviation $|\Delta\bar{\alpha}|_{tol}$ [40].

For mono-dispersed solid-gas flows with a particle size distribution, the grid must, in general, be designed for the coarsest particles in the system. Since the continuum constraints are correlated with the cube of the particle diameter, it is likely that if Equation (17) or (18) is satisfied for the coarsest particles, then it is satisfied for all the particles in the system. This is also physically reasonable since for similar $\bar{\alpha}$, an averaging volume can accommodate more fine particles than coarse particles, resulting in a better continuum model for the former. Similarly, if multiple solid phases (for instance, biomass in a sand bed) are represented as continua, the constraint must be examined for all the solid phases. The constraint will necessarily depend on the size and average volume fraction ratios of the solid particles to account for percolation effects. Even though size distribution/shape effects have not been considered in this study, this analysis is useful for determining the maximum possible grid resolution. Although the final resolution will be specific to the application geometry, flow and particles, it must be emphasized again that simulations using a grid resolution not conforming with constraining Equations (17) or (18) violate the continuum assumption of the TFM and may yield unphysical predictions or show poor convergence.

3.3. Numerical Approach

The numerical technique is based on the SIMPLE (Semi-Implicit Method for Pressure Linked Equations) algorithm on a staggered grid where the velocity components are calculated for points that lie on the boundaries of the control volume [41]. The governing equations are spatially discretized using the finite-volume technique based on central differencing for the diffusion terms and the use of the superbee flux limiter (TVD scheme) for the convection terms, both being second order accurate. The velocity field for each time step is first predicted using the discretized momentum equations based on the pressure field at the end of the previous time step. The predicted velocity field is then iteratively corrected by mass balance (continuity) as well as the volume fraction correction equation to maintain incompressibility of the solid phase in densely packed regions of the bed. The inter-phase coupling is done using the Partial Elimination Algorithm (PEA) [42]. All the scalar variables are updated once the conservative velocity field has been established.

MFiX uses a variable time step which is automatically adjusted to reduce the run time. The initial time step is $10^{-7}s$. Adjustments in the time step are made based on the iteration count for previous time steps. Typically, the maximum time step achieved in the present simulations is on the order of $10^{-4}s$; very high time steps result in unstable calculations. The forward Euler method is used for time marching. More details regarding the time marching, discretization technique and numerical algorithm can be found in [43].

The appropriate wall boundary condition and the centerline treatment are discussed in the following sections.

3.4. Wall Boundary Condition

Fluidization begins when air at ambient conditions is passed though a static bed of fine particles. At the walls, the no-slip boundary condition is employed for the gas phase while the Johnson-Jackson partial-slip model [14] is used for the solid phase in conjunction with the full transport equation for the granular energy given by Equation (8). The Johnson-Jackson model sets the boundary condition for both the solids velocity and the granular temperature for each solid phase. These boundary conditions have been used for all simulation results presented in Sections (4.1) and (4.2). On the other hand, in Section (4.3), all simulation results using the cylindrical or Cartesian grids use the simplified algebraic model for the granular energy, given by Equation (9), since the implementation of the full transport equation on the Cartesian grid [27] is still under development. For these simulations, the solid velocity gradient vanishes at the walls (free-slip) while the gas phase still satisfies no slip. Even though the wall boundary condition is not modeled accurately (using the Jackson-Johnson formulation), it is shown that for the current application, both models are in reasonable agreement.

3.5. Centerline Treatment

In addition to the wall boundary conditions discussed above, special treatment is required at the center of the cylindrical grid to close the conservation equations. As discussed before, this is a numerical artifact of the cylindrical coordinate system. Conventionally, for predicting the radial velocity at the center, the zero-normal flow, i.e. zero-radial velocity condition has been used. Mathematically, this is represented as

$$V_{r,\frac{1}{2}jk} = 0 \qquad (19)$$

7

However, imposing this condition leads to the accumulation of solid particles at the bed center consequently obstructing the flow of gas bubbles. For the present study, three separate radial velocity treatments have been considered. All three cases are presented in Figure (4). One of the earliest solutions, Scheme A in Figure (4), was proposed by Eggels et al. [44] where the centerline radial velocity was predicted based on the diametrical average given by

$$V_{r,\frac{1}{2}jk} = \frac{V_{r,\frac{3}{2}jk} - V_{r,\frac{3}{2}jk+\frac{N_\theta}{2}}}{2} \tag{20}$$

Fukagata and Kasagi [31] combined their conservative scheme with the flux-based formulation proposed by Verzicco and Orlandi [45] which yielded the following centerline radial velocity, Scheme B in Figure (4):

$$V_{r,\frac{1}{2}jk} = V_{r,\frac{3}{2}jk} \tag{21}$$

Recognizing that both Scheme A and Scheme B are multi-valued schemes, i.e the centerline radial velocity predicted for all center cells in a cross-section may not represent a unique Cartesian velocity, Fukagata and Kasagi [31] proposed a single-valued scheme, Scheme C in Figure (4), based on the flow-field around the centerline, in particular, the azimuthal velocity components. This algorithm is shown to be second order accurate with respect to momentum conservation [31]. For the gas phase, the average Cartesian velocity at the center (of the cross section) is given by

$$\bar{V}_{gx,j} = -\frac{2}{N_\theta} \sum_k V_{g\theta,1jk+\frac{1}{2}} \ sin\theta_k \tag{22}$$

$$\bar{V}_{gz,j} = \frac{2}{N_\theta} \sum_k V_{g\theta,1jk+\frac{1}{2}} \ cos\theta_k \tag{23}$$

The radial velocity is then computed for each cell as follows

$$V_{gr,\frac{1}{2}jk} = \bar{V}_{gx,j} \ cos\theta_k + \bar{V}_{gz,j} \ sin\theta_k \tag{24}$$

Similarly, Equations (22) - (24) can be re-written for all the solid phases (m = 1,M). While all the three schemes show similar predictions for relatively high grid resolutions, only results using the single-valued scheme, Scheme C, are presented in this paper since it predicts a unique Cartesian velocity at the center.

Meanwhile, using a staggered grid is also beneficial because the axial velocity and the scalar variables (pressure, granular temperature) are not computed (predicted) at the centerline. Thus, using a centerline condition for the radial velocity does not affect the accuracy of the other variables since they will be solved for using the remaining discretized momentum and scalar equations. For these flow variables, the free slip condition is employed, i.e. the gradient at the center vanishes to prevent stresses from reaching unphysical values. For the gas axial velocity (and similarly others), this is imposed using

$$V_{gy,0j+\frac{1}{2}k} = V_{gy,1j+\frac{1}{2}k} \tag{25}$$

as also described in Figure (5) for the two cells P and Q. Since the centerline forms an edge on the computational domain, this condition is convenient to implement but does not transfer any information across the center, i.e. in this case, the axial velocity at P is not directly influenced by the axial velocity at Q even though there is no physical boundary between P and Q. Alternatively, a more physical approach would be to couple P and Q such that

$$V_{gy,0j+\frac{1}{2}k+\frac{N_\theta}{2}} = V_{gy,1j+\frac{1}{2}k} \tag{26}$$

i.e. $V_{gy,P} = V_{gy,Q'}$ and likewise for all center cells. Simulations using the grid resolution study in Section (4.1) for both inlet superficial velocities show that the difference in the predictions using the conditions given by Equations (25) and (26) is less than 2%. This is expected since the cells at the center of the cylindrical grid are extremely small and hence, spatial variation in the flow variables in these cells is likely to be insignificant. The use of the free slip condition for the present application can, therefore, be justified for the axial velocity and all scalar variables.

4. Results and Discussion

In Section 4.1, a grid refinement study is presented and predictions are compared with experimental measurements of the bed expansion and the cross-sectional void fraction profiles to validate the numerical approach. The appropriate centerline treatment is implemented and its impact is shown in Section 4.2. Finally in Section 4.3, the cylindrical grid and the Cartesian grid are compared in terms of the accuracy of prediction as well as computational cost. Unless stated otherwise, simulation results presented are time averaged over 40s, after it was verified that time averaging over 50s (as in the experiments) did not yield significant differences. Note that the fluidized bed reaches a statistically steady state after 2s, and hence, the first 2s are discounted from the time averaged results to remove fluidization startup effects.

4.1. Resolution Study and Validation

The fluidized bed used in the experiments is 1.5 m high. The computational domain has been limited to 0.6 m and 0.8 m for the bubbling and slugging fluidization cases, respectively. This is to reduce the computational cost of the simulations, and is only possible because in the selected working conditions, the solid particles do not reach the respective elevations. The axial resolution used for all simulations is 5 mm which corresponds to 120 and 160 axial cells for the two cases. Note that a cross-sectional resolution of $i \times j \times k$ represents i radial cells, j axial cells and k azimuth cells for the cylindrical grid while for the Cartesian grid, this corresponds to j axial cells and i and k cross-sectional diametrical cells (along the x- and z- axes, respectively).

A radial grid resolution study using 12 azimuthal cells for both the bubbling (V_o=0.54 m/s) and slugging (V_o=0.80 m/s) fluidization cases using the cylindrical grid is presented in Figure (6). All resolutions (12 to 20 radial cells) show good quantitative agreement with experimental data, although radial grids coarser than 18 cells do not capture the trend near the wall accurately. The azimuthal grid resolution, as shown in Figure (7), is done using 18 radial cells. The time-average void fraction profiles using the two grids are comparable. The appropriate cylindrical grids 18 x 120 x 12 and 18 x 160 x 12 (for the bubbling and slugging fluidization cases, respectively) also predict the experimentally measured bed height with reasonable accuracy, as shown in Figure (8), validating the numerical model.

Direct comparison of cylindrical 3D and Cartesian 3D simulations is non-trivial. One approach is to compare the simulation results keeping the total number of cells approximately the same for both the grids, i.e. simulations using the cylindrical grid $18 \times 120 \times 12$ (say, for the bubbling fluidization case) be compared with the Cartesian grid $15 \times 120 \times 15$ (note: 15 diametrical cells). However, with this cross-sectional resolution, the resulting Cartesian grid is too coarse (25 times the particle diameter) and hence, cannot predict the hydrodynamics accurately [35, 39]. On the other hand, a Cartesian grid with identical cross-sectional resolution as the cylindrical radial grid may be used, i.e. simulations using the cylindrical grid $i \times j \times k$ be compared with the Cartesian grid $2i \times j \times 2i$. The final grid resolutions used for subsequent analysis are presented in Table (2). Using the cylindrical cross sectional resolution 18×12, typical time instant void fractions for the bubbling and slugging fluidization cases are shown in Figures (9) and (10), respectively. Figure (9) shows that bubbles are formed at the bottom of the bed and increase in size as they move up, through coalescence. On the other hand, larger bubbles (slugs) can be seen in Figure (10) which is expected with increasing inlet superficial velocity. Note that the cylindrical grid with the centerline treatment discussed in Section 4.2.1 has been used for these time instant void fraction profiles.

4.2. Cylindrical 3D Simulations

Simulating solid-gas fluidization using cylindrical grids presents complexities not only because of the additional treatment at r=0, but also the significantly small sized cells near the center. The following sections examine these two concerns.

4.2.1. Centerline Treatment

While the predictions using the existing model are in good agreement with the experimental measurements, there is, however, a discrepancy at the center. This is evident from Figure (11), which shows a zoom-in of the grid resolution study presented in Figure (6) near the center. The distinct *dip* in the profile at the bed center is reflective of excess solid holdup and a consequence of imposing the zero-radial velocity condition at the center. This study further justifies the need for appropriate centerline treatment.

Of the several schemes analyzed in Section (3.5), Scheme C, given by Equations (22) - (24), has two distinct advantages: it predicts a unique Cartesian velocity at the center and is also second order accurate with respect to momentum conservation [31]. Hence, only simulation results with Scheme C are presented. A comparison

of the predicted time average void fraction along the axial height of the fluidized bed using the two centerline conditions: zero radial velocity and Scheme C, is shown in Figure (12). The accumulation of the solid particles can be distinctly observed along the axis of the bed for simulations using the zero radial velocity centerline condition. The same can also be visualized through a cross sectional contour plot of the time average void fraction, as shown in Figure (13). Finally, comparing the predictions with experimental measurement between 14.3 and 18.1 cm as shown in Figure (14), it is evident that by relating the centerline velocity to the surrounding flow-field, the unphysical accumulation of solid particles at the center is avoided.

4.2.2. Using Non-Uniform Radial Grid

As discussed previously in Section 3.2, the solid phase continuum model for the TFM may be violated when using extremely small grid cells, especially near the center of the cylindrical grid. Thus, there exists an upper bound on the grid resolution, i.e. a lower bound on the grid size. On the other hand, Figure (6) shows that simulations with very coarse grids may not predict the hydrodynamics accurately. Finding the optimum grid resolution can, thus, be tricky for simulating small lab experiments where the bed diameter-particle size ratio is small. One possible solution to this problem when using the cylindrical grid is to utilize a non-uniform radial grid, in which the grid is refined at the walls while kept relatively coarse near the center to prevent the cells from becoming exceedingly small. The finest resolution (at the walls) must capture the wall effects accurately and may be determined by comparing different radial grid resolutions, while the resolution at the bed center is constrained by the continuum model assumption given in Equation (17). A limitation with this approach, however, is that within the framework of *MFiX*, implementation of higher-order schemes is based on the Normalized Variable Formulation (NVF) methodology which assumes grid uniformity. Therefore, for the present study, second order global accuracy for the momentum equations is strictly only ensured on a uniform grid. However, by comparing the results with the Normalized Variable and Space Formulation (NVSF) methodology, Darwish and Moukalled [46] demonstrated that using second-order NVF on a non-uniform grid only results in minor accuracy losses. The loss in accuracy can further be mitigated by limiting the non-uniformity in the grid (i.e. the spread of cell sizes between the wall and the center) and employing a locally uniform grid where accurate flow computation is essential i.e. at the walls in the present study.

Keeping the above factors in mind, a non-uniform grid is implemented such that the radial resolution decreases from 3 mm at the wall to 4.5 mm at the center keeping the radial cell count to 18, as in the uniform radial grid case (radial resolution 3.8 mm). The average increment in the radial cell size (from the walls to the center) in the non-uniform grid is, thus, less than 3%. Considering that the grid used in [46] is highly non-uniform while the present case is restricted to gradual grid non-uniformity only along the radial direction, it is reasonable to assume that even though global accuracy may not be strictly second order, any loss in accuracy is negligible. Note that the azimuthal and axial grids are kept uniform throughout. Figure (15) compares these two cases: the uniform radial grid with the non-uniform radial grid. Results using the non-uniform radial grid show more accurate predictions not only in the bed interior but also close to the walls.

4.3. Cylindrical 3D v/s Cartesian 3D Simulations

The Cartesian grid using the Cut-Cell approach, as described by Figure (2b), makes use of curved or sloping boundaries i.e. computational cells at the physical boundary are truncated to conform to the cylindrical bed. This makes modeling rather complex especially at the physical boundary. While there has been considerable progress in developing this tool, implementation of the full transport equation for the conservation of granular energy, given by Equation (8), on the Cartesian grid is still in progress. Therefore, simulations using the cylindrical and Cartesian grids in this section are based on the algebraic equation for the transport of granular energy, given by Equation (9), even though this formulation does not appropriately handle the wall boundary condition (Johnson-Jackson boundary condition). For the present study, however, it is shown in Figure (16) for the bubbling fluidization case that the algebraic equation may be used for comparing the accuracy and computational cost of the two grids. A similar comparison is observed for the slugging fluidization case as well although it is not shown for the sake of brevity. Note that for all simulations presented in the previous sections, the full transport equation for conservation of granular energy is used.

A comparison of the results obtained using the cylindrical and Cartesian grids is shown in Figures (17) and (18). The radial resolution for both the grids is 3.8 mm (uniform). Overall, the time average void fraction using the two grids for both the bubbling and slugging fluidization cases is in reasonable agreement although the cylindrical grid shows more solid concentration close to the walls. This is also reflected through Figure (19) which shows that the Cartesian grid underpredicts the cross sectional void fraction upto 8 %. One possible reason is that the Cut-Cell approach approximates the boundary by truncating and discarding *small* cells,

10

i.e. the domain boundary does not perfectly align with the physical boundary. The total computational time for the two grids is presented in Table (3). Both fluidization regimes are simulated almost 10 times faster on the cylindrical grid than the Cartesian grid; the disparity primarily due to the higher number of cells required to simulate the bed using the latter with identical radial resolution as the cylindrical grid. For such applications, as well as complex mixing and segregation studies, the skewed aspect ratio of the cylindrical grid cells is computationally beneficial since high radial resolution is essential for predicting the flow hydrodynamics accurately.

5. Conclusion

The Two-Fluid Method is used to simulate solid-gas fluidization in a cylindrical bed. Through the present study, the accumulation of solid particles at the center is investigated and attributed to imposing the zero radial velocity condition. By introducing a single-valued scheme relating the centerline radial velocity to the surrounding flow field, this excess solids hold-up is avoided and significant improvement in the predicted hydrodynamics is observed, especially near the center. Another concern with the use of a cylindrical grid is the presence of extremely small cells near the bed center. Care must be taken while using highly resolved grids since the presence of these cells may violate the continuum model assumption for the solid phase and consequently, yield unphysical results or slow convergence. Recognizing that accurate prediction of the hydrodynamics close to the wall requires high radial resolution, using a non-uniform radial grid is proposed. In this case, the radial resolution is gradually increased from the bed-center to the wall. It is observed that predictions are in better agreement with experiments as compared to the uniform resolution case.

The third issue addressed in this study is the choice of coordinate system for such applications. One advantage with the cylindrical grid is that the computational domain aligns perfectly with the boundary removing the need for any approximations as would be the case with the Cartesian Cut-Cell technique. This makes predictions more accurate; the disparity in results between the two grids likely to be significant for small laboratory scale beds. Moreover, the cylindrical grid is also shown to be more efficient. This is because high radial resolution is preferred over high azimuthal resolution, unlike the Cartesian grid where both cross-sectional axes must be equally well resolved. Therefore, the Cartesian grid has more cells in the domain and since the computational cost is a strong function of the total cells in the domain, the Cartesian grid is an order of magnitude slower than the cylindrical grid. Thus, even though the Cartesian grid can handle complex geometries, it is not as efficient as the cylindrical grid for modeling cylindrical reactor beds.

In general, fluidization may involve multiple solid and gas phases. For multiple solid phases, the grid resolution must be carefully chosen such that the continuum model is valid for each solid phase independently, especially for the center cells. There is, thus, a trade off in the choice of axial, radial and azimuthal resolutions which must be settled based on the particular application, even though the final grid resolution is likely to be limited by the coarsest solid particles in the system. For non-spherical particles (eg biomass), including the shape effects may make the resolution constraining equation more stiff than the ones presented in this paper for spherical particles. The effect of using the single-valued scheme and non-uniform radial grid also has to be further investigated for application to reactive fluidization.

6. Acknowledgment

[1] Daizo Kunii and Octave Levenspiel. *Fluidization Engineering.* 1991.

[2] D. Gidaspow. *Multiphase Flow and Fluidization: Continuum and Kinetic Theory Descriptions.* Boston: Academic, 1994.

[3] J.A.M. Kuipers and W.P.M. van Swaaij. Computational fluid dynamics applied to chemical reaction engineering, in "scientific computing in chemical engineering ii". In *Computational Fluid Dynamics, Reaction Engineering and Molecular Properties*, pages 383–390. Springer, Berlin, 1999.

[4] H Enwald, E Peirano, and A.-E Almstedt. Eulerian two-phase flow theory applied to fluidization. *International Journal of Multiphase Flow*, 22, Supplement:21 – 66, 1996.

[5] Jennifer Sinclair Curtis and Berend van Wachem. Modeling particle-laden flows: A research outlook. *AIChE Journal*, 50(11):2638–2645, 2004.

[6] Y. Tsuji, T. Kawaguchi, and T. Tanaka. Discrete particle simulation of two-dimensional fluidized bed. *Powder Technology*, 77(1):79 – 87, 1993.

[7] B.P.B. Hoomans, J.A.M. Kuipers, W.J. Briels, and W.P.M. van Swaaij. Discrete particle simulation of bubble and slug formation in a two-dimensional gas-fluidised bed: A hard-sphere approach. *Chemical Engineering Science*, 51(1):99 – 118, 1996.

[8] B.H. Xu and A.B. Yu. Numerical simulation of the gas-solid flow in a fluidized bed by combining discrete particle method with computational fluid dynamics. *Chemical Engineering Science*, 52(16):2785 – 2809, 1997.

[9] Nan Xie, Francine Battaglia, and Sreekanth Pannala. Effects of using two- versus three-dimensional computational modeling of fluidized beds: Part i, hydrodynamics. *Powder Technology*, 182(1):1 – 13, 2008.

[10] N.G. Deen M.A. van der Hoef, M. van Sint Annaland and J.A.M. Kuipers. Numerical simulation of dense gas-solid fluidized beds: A multiscale modeling strategy. *Annual Review of Fluid Mechanics*, 40:47–70, 2008.

[11] J.T. Jenkins and S.B. Savage. A theory for the rapid flow of identical, smooth, nearly elastic, spherical particles. *J. Fluid Mech.*, 130:187–202, 1983.

[12] Hayley H. Shen. Stresses in a rapid flow of spherical solid with two sizes. *Particulate Science and Technology*, 2(1):37–56, 1984.

[13] Jianmin Ding and Dimitri Gidaspow. A bubbling fluidization model using kinetic theory of granular flow. *AIChE Journal*, 36(4):523–538, 1990.

[14] P.C. Johnson and R. Jackson. Frictional collisional constitutive relations for granular materials, with application to plane shearing. *Journal of Fluid Mechanics*, 176:67–93, 1987.

[15] M. Syamlal and T.J. O'Brien. Simulation of granular layer inversion in liquid fluidized beds. *International Journal of Multiphase Flow*, 14(4):473 – 481, 1988.

[16] Madhava Syamlal, William Rogers, and Thomas J. O'Brien. *MFIX Documentation Theory Guide*, 1993.

[17] M.J.V. Goldschmidt, R. Beetstra, and J.A.M. Kuipers. Hydrodynamic modelling of dense gas-fluidised beds: comparison and validation of 3d discrete particle and continuum models. *Powder Technology*, 142(1):23 – 47, 2004.

[18] Fariborz Taghipour, Naoko Ellis, and Clayton Wong. Experimental and computational study of gas-solid fluidized bed hydrodynamics. *Chemical Engineering Science*, 60(24):6857 – 6867, 2005.

[19] Antonio Busciglio, Giuseppa Vella, Giorgio Micale, and Lucio Rizzuti. Analysis of the bubbling behaviour of 2d gas solid fluidized beds: Part ii. comparison between experiments and numerical simulations via digital image analysis technique. *Chemical Engineering Journal*, 148(1):145 – 163, 2009.

[20] Tingwen Li, John Grace, and Xiaotao Bi. Study of wall boundary condition in numerical simulations of bubbling fluidized beds. *Powder Technology*, 203(3):447 – 457, 2010.

[21] B.G.M. van Wachem, J.C. Schouten, R. Krishna, and C.M. van den Bleek. Eulerian simulations of bubbling behaviour in gas-solid fluidised beds. *Computers & Chemical Engineering*, 22, Supplement 1(0):S299 – S306, 1998. European Symposium on Computer Aided Process Engineering-8.

[22] Nan Xie, Francine Battaglia, and Sreekanth Pannala. Effects of using two- versus three-dimensional computational modeling of fluidized beds: Part ii, budget analysis. *Powder Technology*, 182(1):14 – 24, 2008.

[23] Schalk Cloete, Stein Tore Johansen, and Shahriar Amini. Investigation into the effect of simulating a 3d cylindrical fluidized bed reactor on a 2d plane. *Powder Technology*, 239(0):21 – 35, 2013.

[24] Mirka Deza and Francine Battaglia. Approximating a three-dimensional fluidized bed with two-dimensional simulations. In *ASME International Mechanical Engineering Congress and Exposition*, 2008.

[25] Tingwen Li, Yongmin Zhang, John R. Grace, and Xiaotao Bi. Numerical investigation of gas mixing in gas-solid fluidized beds. *AIChE Journal*, 56(9):2280–2296, 2010.

[26] Nan Zhang, Bona Lu, Wei Wang, and Jinghai Li. 3d cfd simulation of hydrodynamics of a 150 mw circulating fluidized bed boiler. *Chemical Engineering Journal*, 162(2):821 – 828, 2010.

[27] J.F. Dietiker. *Multiphase Flow with Interphase eXchanges Cartesian Grid User Guide*. National Energy Technology Laboratory, January 2013.

[28] Vikrant Verma, Niels G. Deen, Johan T. Padding, and J.A.M. Kuipers. Two-fluid modeling of three-dimensional cylindrical gas-solid fluidized beds using the kinetic theory of granular flow. *Chemical Engineering Science*, 102:227–245, 2013.

[29] C.C. Pain, S. Mansoorzadeh, and C.R.E. de Oliveira. A study of bubbling and slugging fluidised beds using the two-fluid granular temperature model. *International Journal of Multiphase Flow*, 27(3):527 – 551, 2001.

[30] G.S. Constantinescu and S.K. Lele. A highly accurate technique for the treatment of flow equations at the polar axis in cylindrical coordinates using series expansions. *Journal of Computational Physics*, 183(1):165–186, November 2002.

[31] Koji Fukagata and Nobuhide Kasagi. Highly energy-conservative finite difference method for the cylindrical coordinate system. *Journal of Computational Physics*, 181(2):478–498, September 2002.

[32] Youhei Morinishi, Oleg V. Vasilyev, and Takeshi Ogi. Fully conservative finite difference scheme in cylindrical coordinates for incompressible flow simulations. *Journal of Computational Physics*, 197(2):686–710, July 2004.

[33] Sofiane Benyahia. On the effect of subgrid drag closures. *Industrial & Engineering Chemistry Research*, 49(11):5122–5131, 2010.

[34] Yesim Igci, Arthur T. Andrews, Sankaran Sundaresan, Sreekanth Pannala, and Thomas O'Brien. Filtered two-fluid models for fluidized gas-particle suspensions. *AIChE Journal*, 54(6):1431–1448, 2008.

[35] Simon Schneiderbauer, Stefan Puttinger, and Stefan Pirker. Comparative analysis of subgrid drag modifications for dense gas-particle flows in bubbling fluidized beds. *AIChE Journal*, 59(11):4077–4099, 2013.

[36] Yassir T. Makkawi, Phillip C. Wright, and Raffaella Ocone. The effect of friction and inter-particle cohesive forces on the hydrodynamics of gas-solid flow: A comparative analysis of theoretical predictions and experiments. *Powder Technology*, 163(12):69 – 79, 2006.

[37] S. Benyahia, M. Syamlal, and T.J. OBrien. *Summary of MFIX Equations 2012-1*, January 2012.

[38] M. Coroneo, L. Mazzei, P. Lettieri, A. Paglianti, and G. Montante. CFD prediction of segregating fluidized bidisperse mixtures of particles differing in size and density in gas-solid fluidized beds. *Chemical Engineering Science*, 66(11):2317 – 2327, 2011.

[39] Junwu Wang, M.A. van der Hoef, and J.A.M. Kuipers. Why the two-fluid model fails to predict the bed expansion characteristics of geldart a particles in gas-fluidized beds: A tentative answer. *Chemical Engineering Science*, 64(3):622 – 625, 2009.

[40] A. Celmins. Representation of two-phase flows by volume averaging. *International Journal of Multiphase Flow*, 14(1):81 – 90, 1988.

[41] Suhas V. Patankar. *Numerical Heat Transfer and Fluid Flow*. Hemisphere Publishing Corporation, 1980.

[42] D.B. Spalding. *Numerical computation of multi-phase fluid flow and heat transfer*, pages 139–167. 1980.

[43] Madhava Syamlal. *MFIX Documentation Numerical Technique*, January 1998.

[44] G.M. Eggels, F. Unger, M.H. Weiss, J. Westerweel, R.J. Adrian, R. Friedrich, and T.M. Niewstadt. Fully developed turbulent pipe flow: a comparison between direct numerical simulation and experiment. *Journal of Fluid Mechanics*, 268:175–209, 1994.

[45] R. Verzicco and P. Orlandi. A finite-difference scheme for three-dimensional incompressible flows in cylindrical coordinates. *Journal of Computational Physics*, 123(2):402–414, February 1996.

[46] M. S. Darwish and F. H. Moukalled. Normalized variable and space formulation methodology for high-resolution schemes. *Numerical Heat Transfer, Part B: Fundamentals*, 26(1):79–96, 1994.
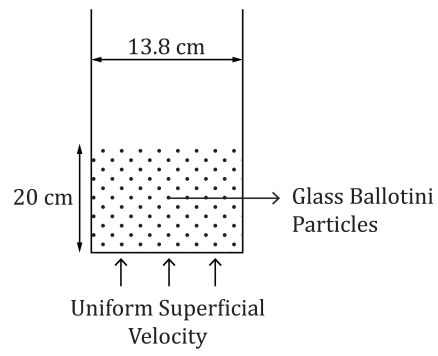
Figure 1: Schematic of the experimental setup [36]

(a)

(b)
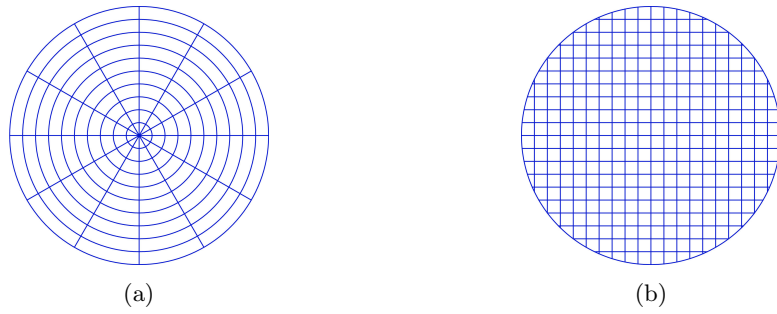
Figure 2: Discretization of the bed cross-section for (a) cylindrical grid and (b) Cartesian grid (Δ r = Δ x = Δ y = 6.9 mm)
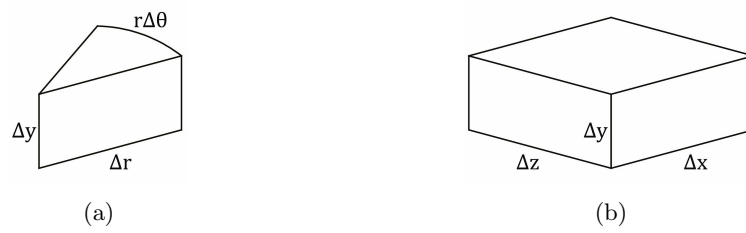
Figure 3: Grid cells at the bed center using (a) cylindrical and (b) Cartesian grid ($\Delta r = \Delta x = \Delta z$)

Scheme A   Scheme B   Scheme C
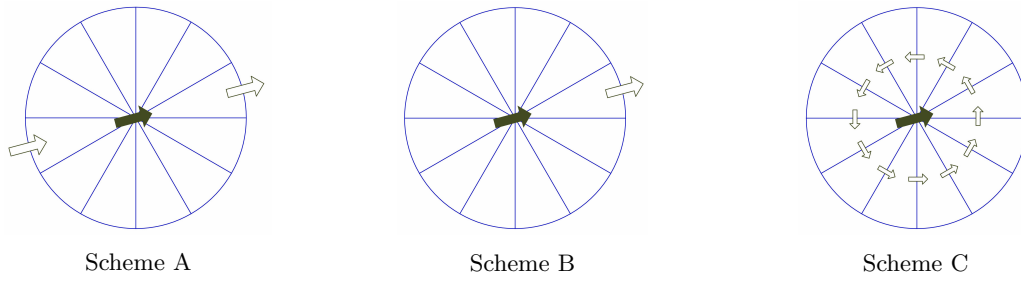
Figure 4: Centerline treatment: The prediction of the centerline radial velocity
(shaded arrows) based on the surrounding flow field (non-shaded arrows)
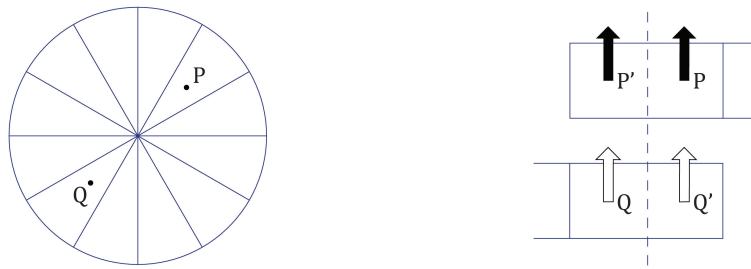
Figure 5: Implementation of the free slip condition for the axial velocity; P' and Q' are *wall* cells for the interior cells P and Q respectively separated by the domain centerline (dashed line)
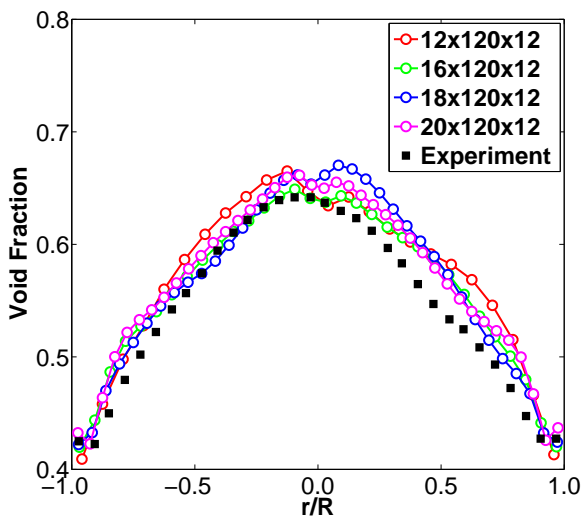
(a) V_o=0.54 m/s
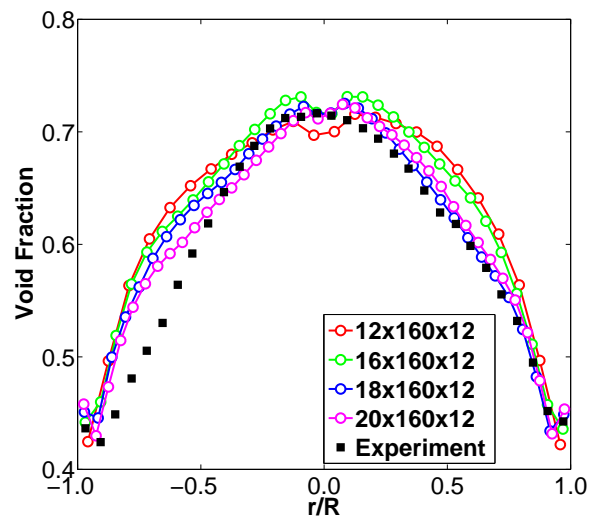
(b) V_o=0.80 m/s

Figure 6: Radial grid resolution study with 12 azimuthal cells based on the time average void fraction using cylindrical 3D grid for (a) bubbling and (b) slugging fluidization at the axial height 14.3 - 18.1 cm
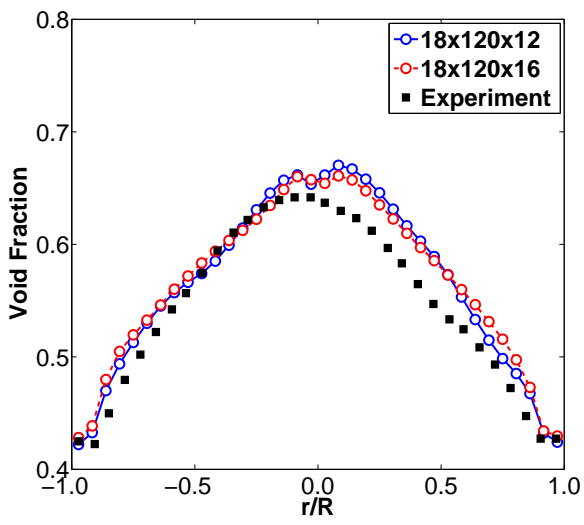
(a) V_o=0.54 m/s
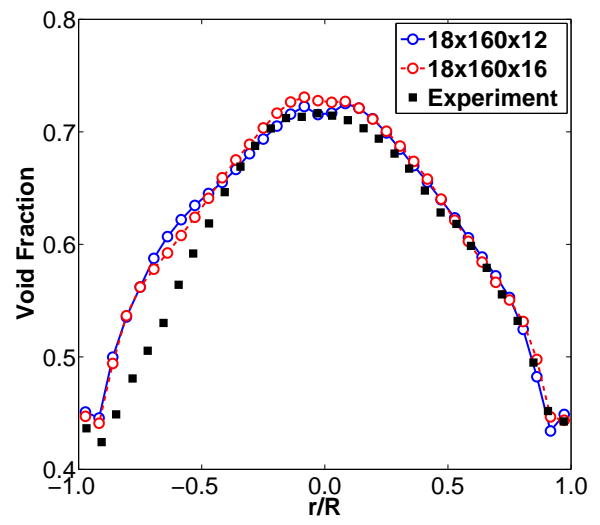
(b) V_o=0.80 m/s

Figure 7: Azimuthal grid resolution study with 18 radial cells based on the time average void fraction using cylindrical 3D grid for (a) bubbling and (b) slugging fluidization at the axial height 14.3 - 18.1 cm
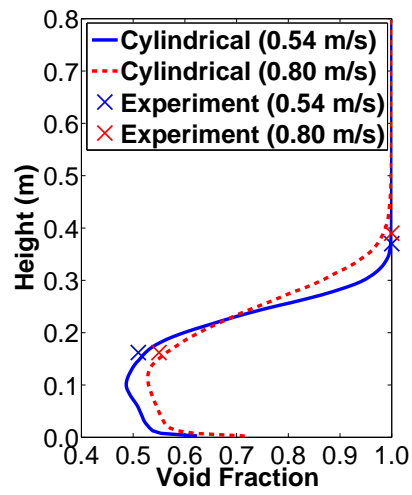
Figure 8: Average cross-sectional void fraction as a function of axial height using the cylindrical grids (18 x 120 x 12) and (18 x 160 x 12) for V_o=0.54 m/s and V_o=0.80 m/s respectively

(a) 15.0 s   (b) 15.5 s   (c) 16.0 s
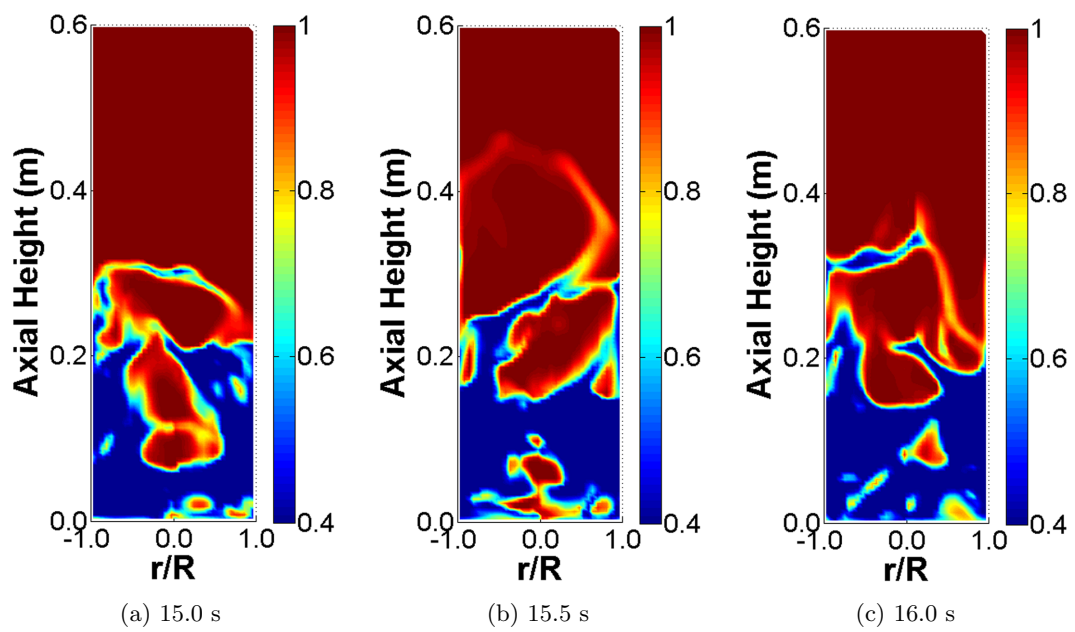
Figure 9: Void fraction along an axial slice in the bed center for $V_0 = 0.54$ m/s at different time instants

(a) 15.0 s   (b) 15.5 s   (c) 16.0 s
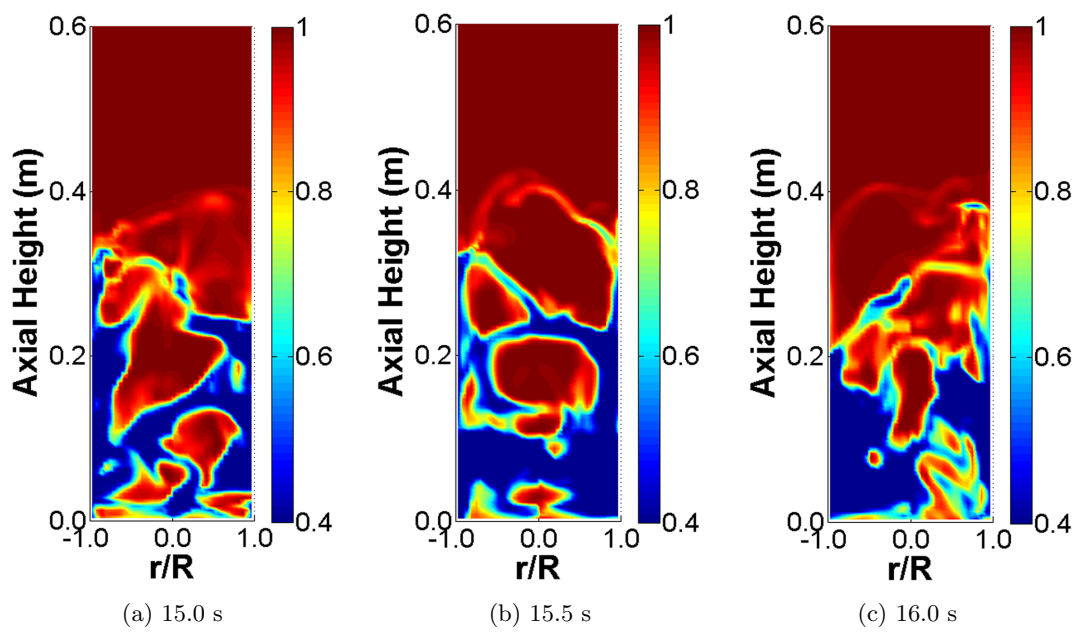
Figure 10: Void fraction along an axial slice in the bed center for $V_0 = 0.80$ m/s at different time instants
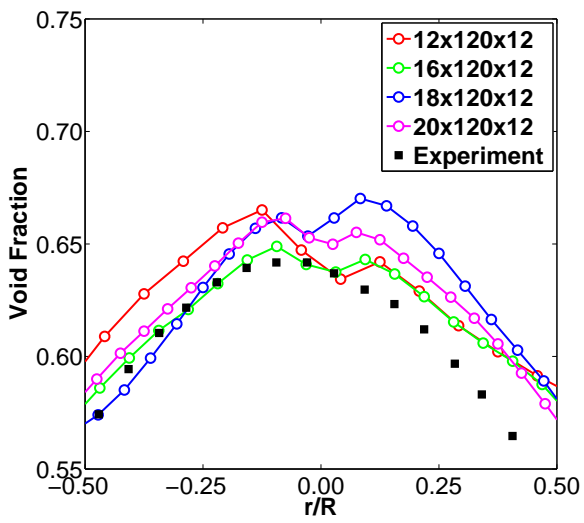
(a) V_o=0.54 m/s
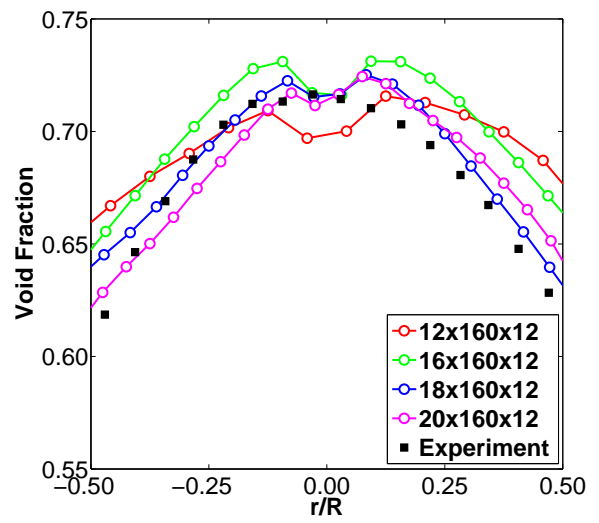
(b) V_o=0.80 m/s

Figure 11: Grid resolution study presented in Figure (6) zoomed in at the center of the bed
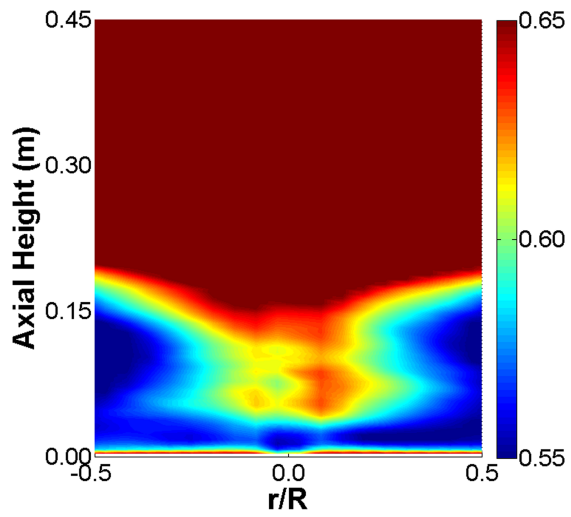
(a) V_o=0.54 m/s, Zero Radial Velocity
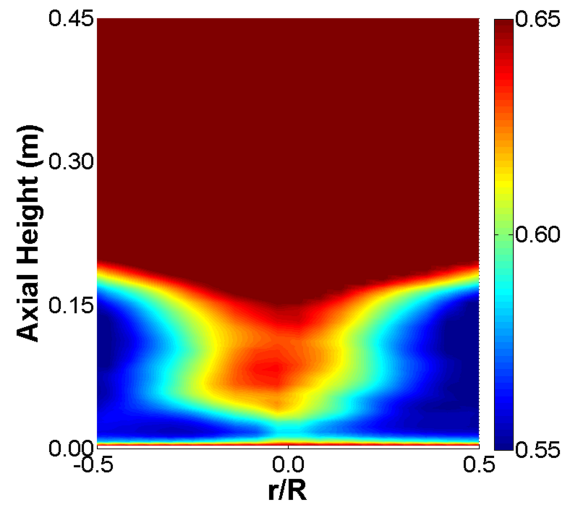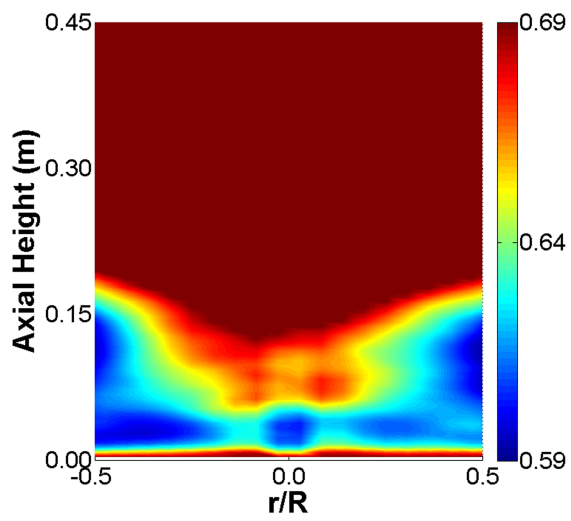
(b) V_o=0.54 m/s, Scheme C

(c) V_o=0.80 m/s, Zero Radial Velocity
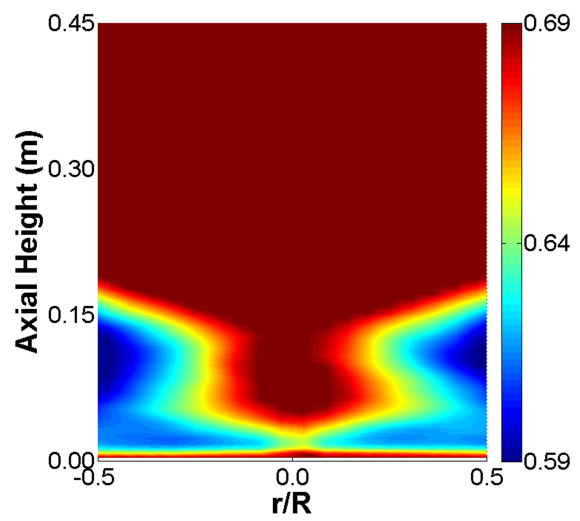
(d) V_o=0.80 m/s, Scheme C

Figure 12: Variation of time average void fraction with axial height for
the centerline condition: Zero Radial Velocity in (a),(c) and Scheme C in (b),(d)
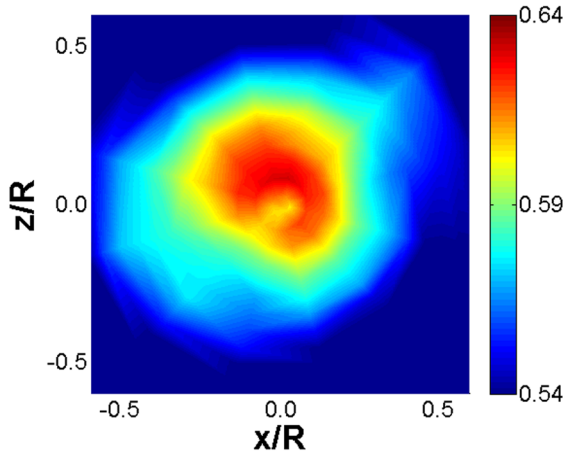
(a) V_o=0.54 m/s, Zero Radial Velocity
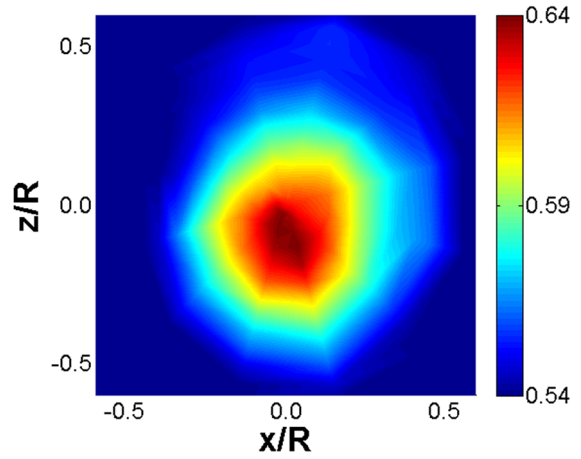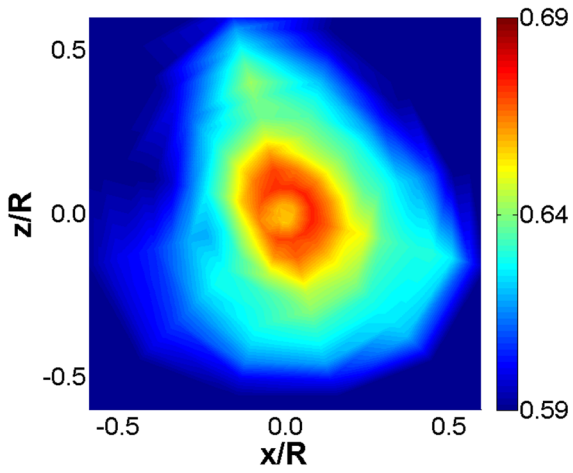
(b) V_o=0.54 m/s, Scheme C

(c) V_o=0.80 m/s, Zero Radial Velocity
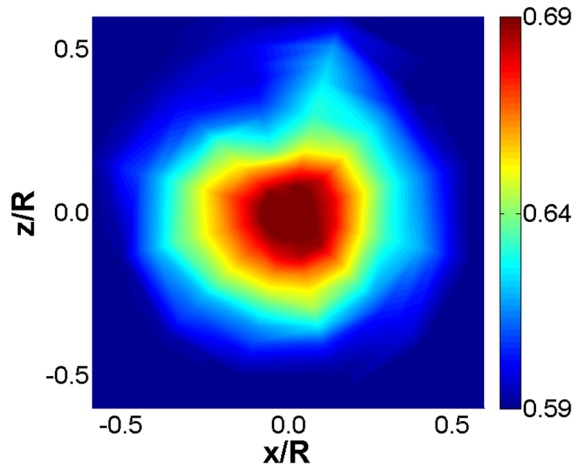
(d) V_o=0.80 m/s, Scheme C

Figure 13: Time average void fraction at axial height = 0.0675 m for
the centerline condition: Zero Radial Velocity in (a),(c) and Scheme C in (b),(d)
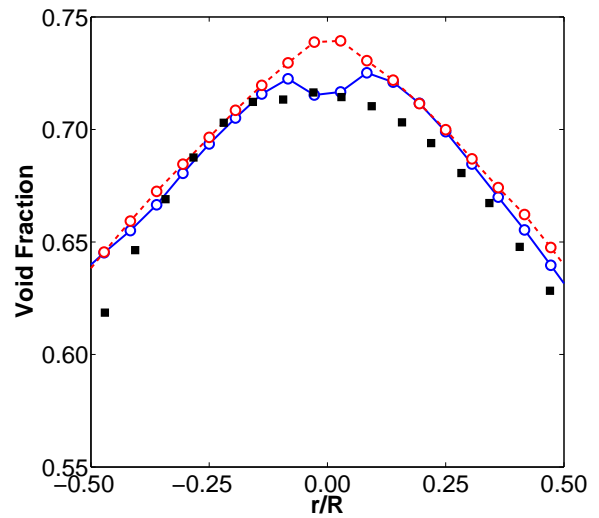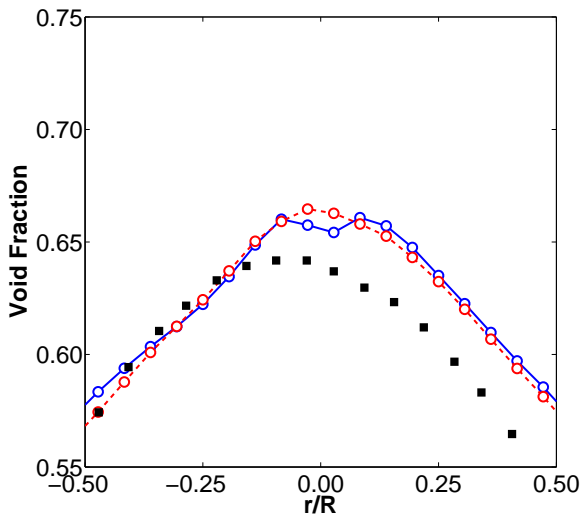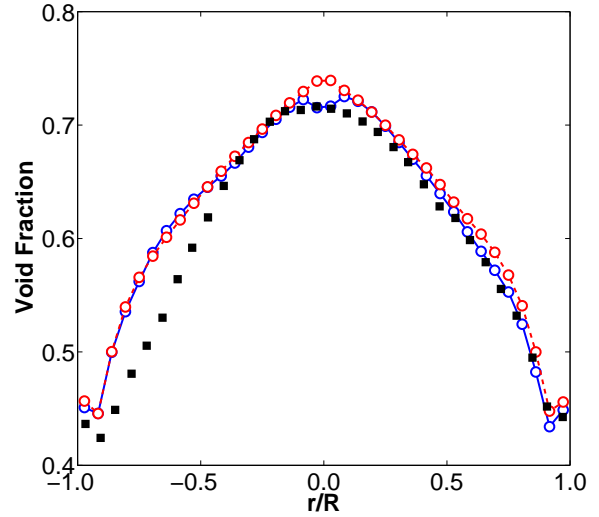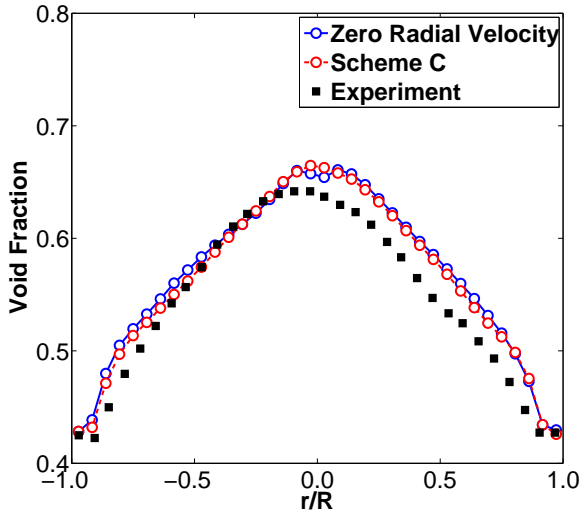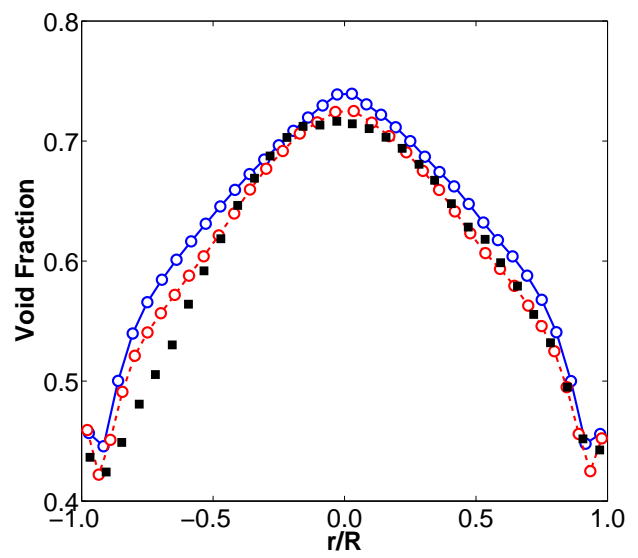
(a) V_o=0.54 m/s, Grid: 18 x 120 x 12   (b) V_o=0.80 m/s, Grid: 18 x 160 x 12

Figure 14: Impact of radial velocity boundary condition at the center of
the cylindrical 3D grid at the axial height 14.3 - 18.1 cm
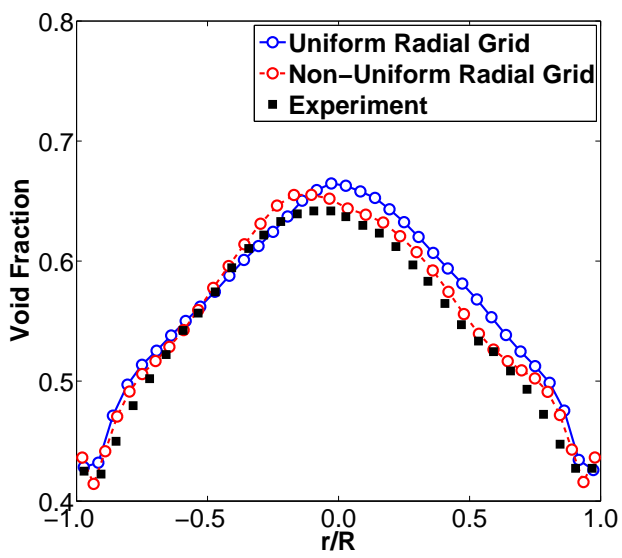
(a) V_o=0.54 m/s, Grid: 18 x 120 x 12   (b) V_o=0.80 m/s, Grid: 18 x 160 x 12

Figure 15: Comparison of uniform and non-uniform radial grids using
the cylindrical 3D grid at the axial height 14.3 - 18.1 cm

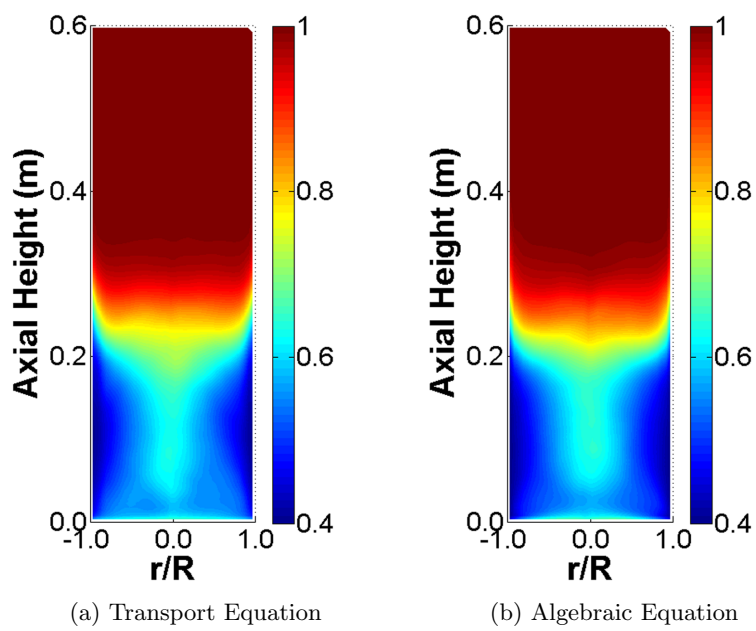(a) Transport Equation   (b) Algebraic Equation

Figure 16: Comparison of the time average void fraction obtained using different models for evaluating the granular temperature. Simulations are performed using the cylindrical 3D grid with $V_0 = 0.54$ m/s

(a) Cylindrical Grid
(18 x 120 x 12)
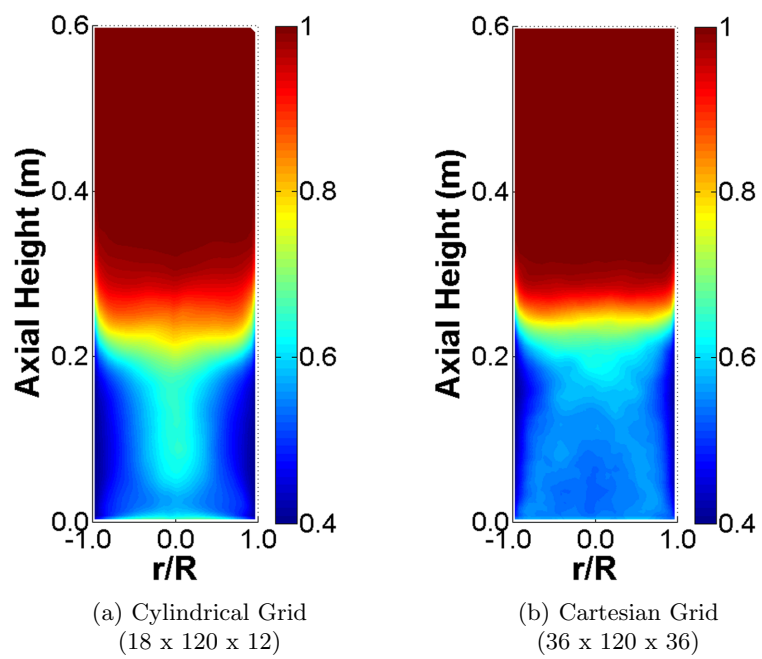
(b) Cartesian Grid
(36 x 120 x 36)

Figure 17: Comparison of the time average void fraction obtained using the two grids for $V_0 = 0.54$ m/s

(a) Cylindrical Grid
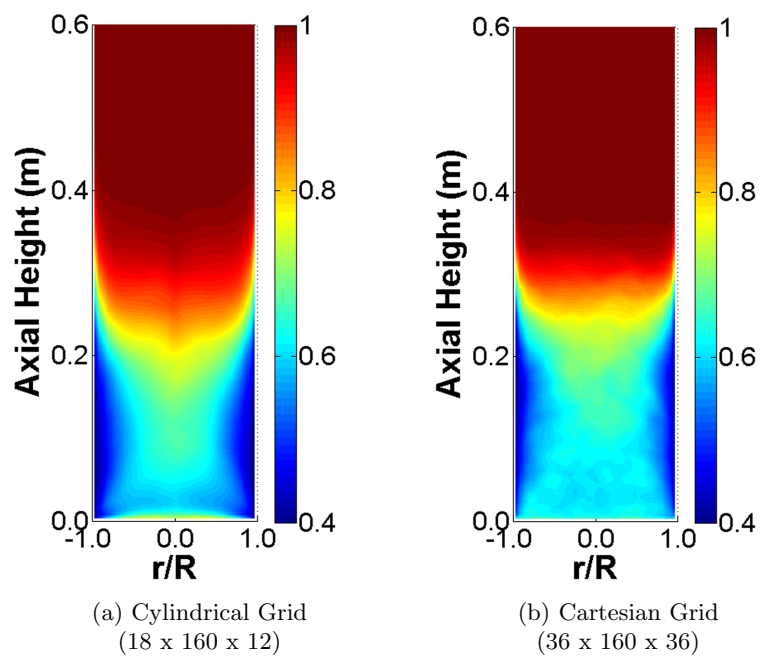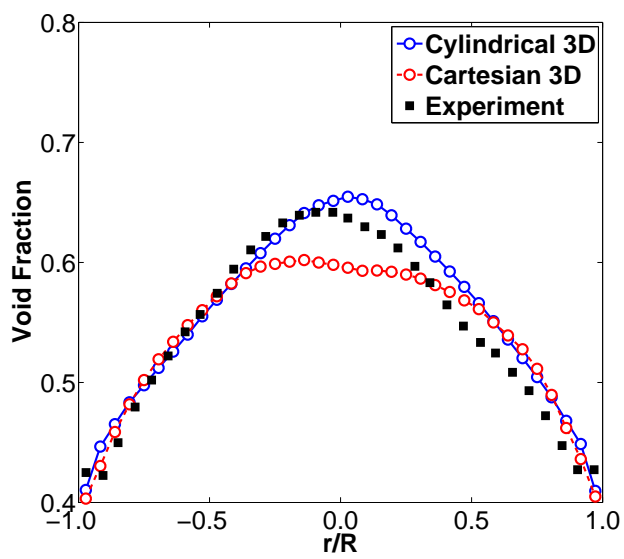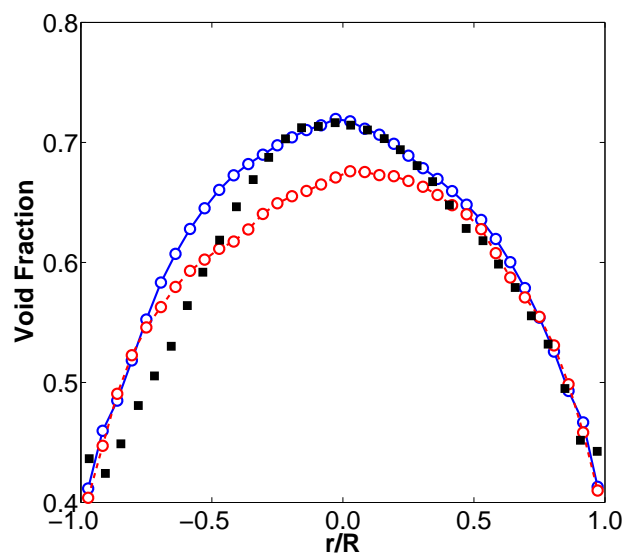(18 x 160 x 12)

(b) Cartesian Grid
(36 x 160 x 36)

Figure 18: Comparison of the time average void fraction obtained using the two grids for $V_0 = 0.80$ m/s

(a) V_o=0.54 m/s, Cylindrical Grid: 18 x 120 x 12
Cartesian Grid: 36 x 120 x 36

(b) V_o=0.80 m/s, Cylindrical Grid: 18 x 160 x 12
Cartesian Grid: 36 x 160 x 36

Figure 19: Comparison of the time average cross sectional void fraction
using the two grids at the axial height 14.3 - 18.1 cm

Table 1: Simulation Parameters

Simulation Time	40 s
Bed Diameter	13.8 cm
Simulated Bed Height	0.6 m / 0.8 m
Particles	Glass Ballotini
	$d_p = 350\,\mu m,\ \rho_p = 2500\,kg/m^3$
Static Bed Height	20 cm
Initial Solid Packing	0.6
Fluidizing Gas	Air (ambient)
Inlet Superficial Velocity	0.54 m/s, 0.80 m/s
Measuring Level	14.3-18.1 cm

Table 2: Final grid resolution based on the grid study

Regime	Superficial Velocity	Cylindrical Grid	Cartesian Grid
Bubbling	0.54 m/s	$18 \times 120 \times 12$	$36 \times 120 \times 36$
Slugging	0.80 m/s	$18 \times 160 \times 12$	$36 \times 160 \times 36$

Table 3: CPU Time for 40s of real time

Regime	Coordinate System	Domain	CPU Time (hrs)
Bubbling	Cylindrical 3D	$18 \times 120 \times 12$	347.6
	Cartesian Cut-Cell 3D	$36 \times 120 \times 36$	3168.4
Slugging	Cylindrical 3D	$18 \times 160 \times 12$	510.2
	Cartesian Cut-Cell 3D	$36 \times 160 \times 36$	4089.9